Electronic Supplementary Information (ESI)

Structural reduced graphene oxide supercapacitors mechanically enhanced with tannic acid

Paraskevi Flouda,[a] Junyeong Yun,[b] Dimitrios Loufakis,[a] Smit A. Shah,[b] Micah J. Green,[b] Dimitris C. Lagoudas,[a,c] and Jodie L. Lutkenhaus [b,*]

a. Department of Materials Science and Engineering, Texas A&M University, College Station, TX 77843, USA.

b. Artie McFerrin Department of Chemical Engineering Texas A&M University, College Station, TX 77843, USA.

c. Department of Aerospace Engineering, Texas A&M University, College Station, TX 77843, USA.

Experimental methods

Materials

Graphite and Kevlar®69 thread were purchased from Bay Carbon and Thread Exchange, respectively. Sulfuric acid (H_2SO_4), potassium hydroxide (KOH), dimethyl sulfoxide (DMSO), potassium permanganate ($KMnO_4$), sodium nitrate ($NaNO_3$), Tris buffer solution (pH 8.5) and Poly(vinyl alcohol) (PVA, Mw 89,000-98,000, 99+% hydrolysed) were purchased from Sigma-Aldrich. Celgard 3501 was provided by Celgard. Carbon paper and phosphoric acid (H_3PO_4, 85% aqueous solution) were purchased from Alfa Aesar. Electrically conductive double-sided tape (XYZ-Axis, 6.35 mm x 32.9 mm) was purchased from 3M.

Fabrication of composite electrodes

Graphene oxide (GO) was synthesized from graphite using a modified Hummers method as previously reported.[1] To functionalize GO with tannic acid, desirable amounts of GO aqueous dispersion (1 mg/ml) were mixed with tannic acid in a basic solution of Tris buffer (pH: 8.5). The mixture was stirred for 24 h at room temperature. Finally, the mixture was filtered using Whatman filter paper (2.5 pore size and 55 mm diameter) and washed in ethanol:water (1:1 v:v mixture).[2] The obtained powder was dried at 60 ^oC overnight under vacuum and re-dispersed in DMSO. Branched aramid nanofibers (BANF) were produced by the dissolution of chopped Kevlar® fiber (0.5 g) in DMSO (50 ml) and KOH (0.5 g).[3] Composite thin films of GO-TA and BANF were fabricated using vacuum filtration as described in previous reports. The composites were further dried at 80 ^oC for three days and thermally reduced at 200 ^oC under vacuum.[4, 5]

Fabrication of all-solid-state flexible supercapacitor

First a H_3PO_4-PVA gel electrolyte was synthesized. PVA (5 g) and milli-Q-water (50 ml) were mixed and stirred at 130 ^oC until a clear solution was obtained. The solution was then cooled

to room temperature. H_3PO_4 (3.46 ml) was added and stirred for 1 hour at room temperature. The composite electrodes (rGO-TA/10 wt% BANF/Fe^{3+}) were cut into 0.5 cm x 3 cm strips and were attached to commercial conductive tape used as a current collector, respectively. A pre-cured at room temperature H_3PO_4-PVA film was cut into a 0.7 cm x 3.5 cm strip. Then, we applied uncured H_3PO_4-PVA gel electrolyte to both sides of this pre-cured H_3PO_4-PVA film and the prepared electrodes were carefully attached to each side. The all-solid-state flexible supercapacitor was obtained after drying for 20 ^oC at room temperature. The flexible device had a total thickness of ~0.64 cm and mass of ~18.5 mg (current collector, electrodes, and electrolyte).

Material Characterization

The morphology of the composite films was examined using scanning electron microscopy (JEOL, SEM). X-ray photoelectron spectroscopy (XPS) was conducted using an Omicron ESCA Probe with Mg Ka radiation (hm = 1253.6 eV). Survey scans were collected at 100-1100 eV with steps of 1.0 eV and 50 ms dwell time. High resolution scans were collected with steps of 0.05 eV and 200 ms dwell time. The C1s peak for sp^2-hybridized carbon atoms (284.5 eV) was used to calibrate all spectra. Shirley background correction, gaussian-lorentzian peak shape fitting were applied and the FWHM of the peaks was constrained. Raman spectroscopy was conducted using a Horiba Jobin-Yvon Lab Ram HR with 514 nm excitation. X-ray diffraction was conducted using a Brucker D8 X-ray. The X-ray source was Cu (Ka, λ = 1.541 Å) and the diffractograms were obtained at 2θ range 5^o – 50^o. A TA Q50 analyzer was used to conduct thermogravimetric analysis under N_2 gas (TGA). The samples were heated and isothermally held at 80 ^oC with a rate of 10 ^oC/min for 2 h, followed by heating to 600 ^oC.

Mechanical and Electrical Characterization

Strips of the composites were used for tensile testing using a DMA Q8OO. A strain rate of 0.1 %/min and a preload force of 0.02 Nt were used. All experiments were contacted at room temperature and humidity (~23 ^{o}C and 30-35 %). Young's modulus, ultimate tensile strength, toughness, and ultimate strain were calculated as previously reported.[5] Creep tests were conducted at 40 MPa with a creep and recovery time of 60 min each. The electrical measurements were performed using a digital multimeter (Keithley 2110). Four copper wires (leads) were attached to the surface of the samples using conductive silver paste. The distance between the leads was measured using a digital calliper (Fowler 54-100-067-1 Ultra-Cal V) and the thickness of the electrode was measured *via* cross-sectional SEM. The conductivity of the samples was calculated from the resistance output of the multimeter. The conductivity tests were carried out in room temperature and humidity, and the samples were free of strain.

Electrochemical Characterization

Supercapacitors were tested using two-electrode (diameter: 16 mm, mass loading: 1.5 - 2 mg/cm^2) symmetric coin cells with 6M KOH as the electrolyte. Celgard polypropylene (19 mm) was used as the separator and stainless steel as the spacer and spring. Carbon paper was used as the current collector. Electrochemical characterization was performed using a Gamry potentiostat (Gamry Interface 1000). Cyclic voltammetry was performed at various scan rates (1-100 mV/s) within a potential window of 0-1 V. Galvanostatic charge-discharge experiments were conducted at various current densities (0.2-2 A/g). The specific capacitance was calculated for both cases as previously reported.[4, 5]

Supporting figures

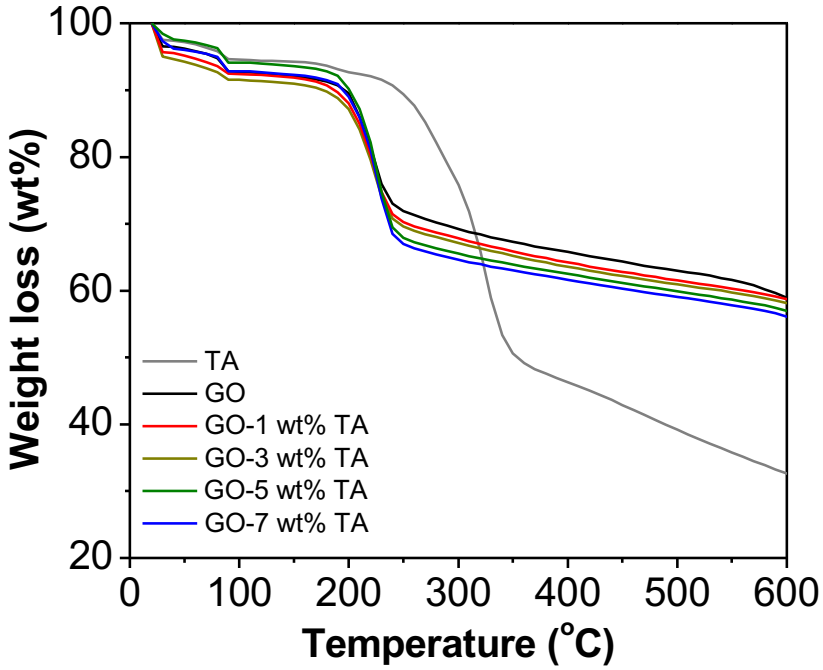

Fig. S1 Thermogravimetric analysis (TGA) curves for TA, GO, GO-1 wt% TA, GO-3 wt% TA, GO-5 wt% TA, and GO-7 wt% TA. The samples were isothermally kept at 80 °C for 2 h and then heated to 600 °C. TGA was conducted under N_2 atmosphere with a heating rate of 10 °C/min.

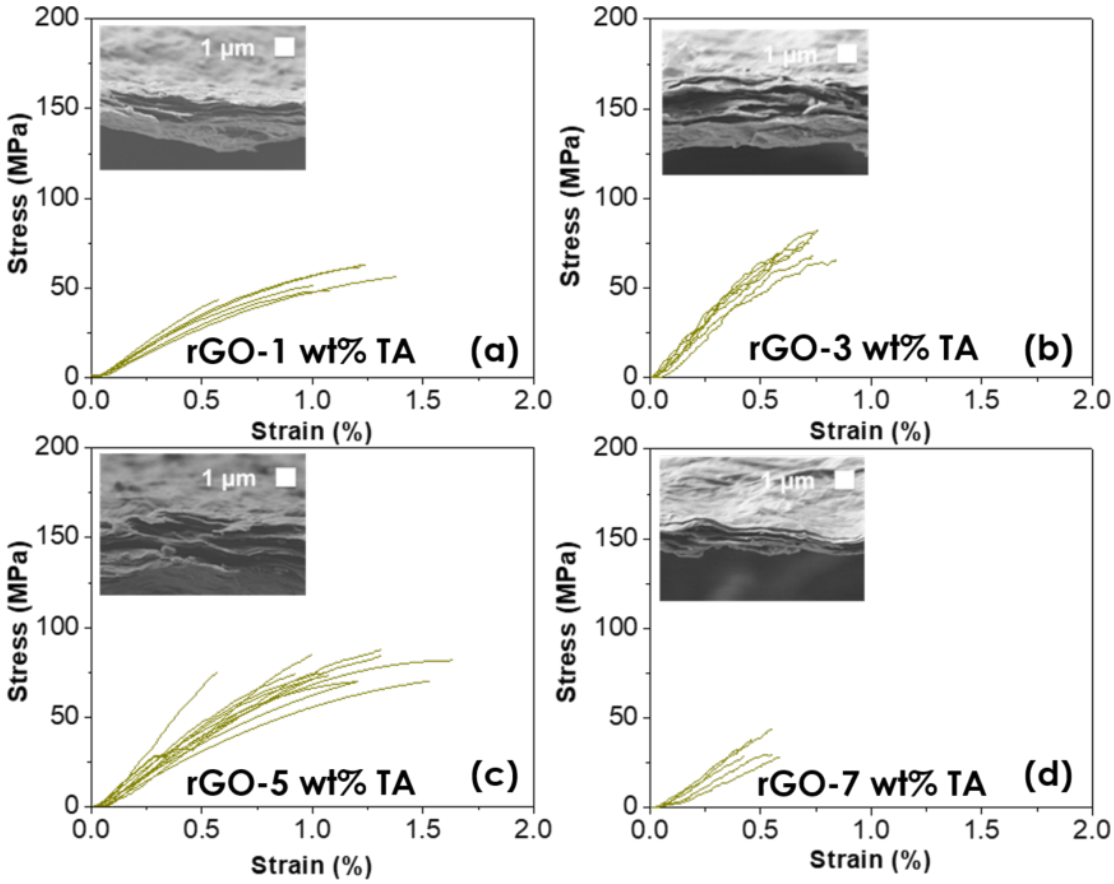

Fig. S2 Stress-strain curves for (a) rGO-1 wt% TA, (b) rGO-3 wt% TA, (c) rGO-5 wt% TA, and (d) rGO-7 wt% TA. Insets show cross-sectional SEM images of the electrodes (no BANFs).

Table S1 XPS analysis for rGO/10 wt% BANF, rGO-TA/10 wt% BANF, rGO-TA/10 wt% BANF/Ca^{2+}, and rGO-TA/10 wt% BANF/Fe^{3+}.

at %	**rGO/10 wt% BANF**	**rGO-TA/10 wt% BANF**	**rGO-TA/10 wt% BANF/Ca^{2+}**	**rGO-TA/10 wt% BANF/Fe^{3+}**
C	78.0	72.3	70.2	67.4
O	17.1	23.0	23.8	25.4
N	4.9	4.7	4.5	4.3
Ca	-	-	1.5	-
Fe	-	-	-	2.9
C/O	4.6	3.1	2.9	2.7

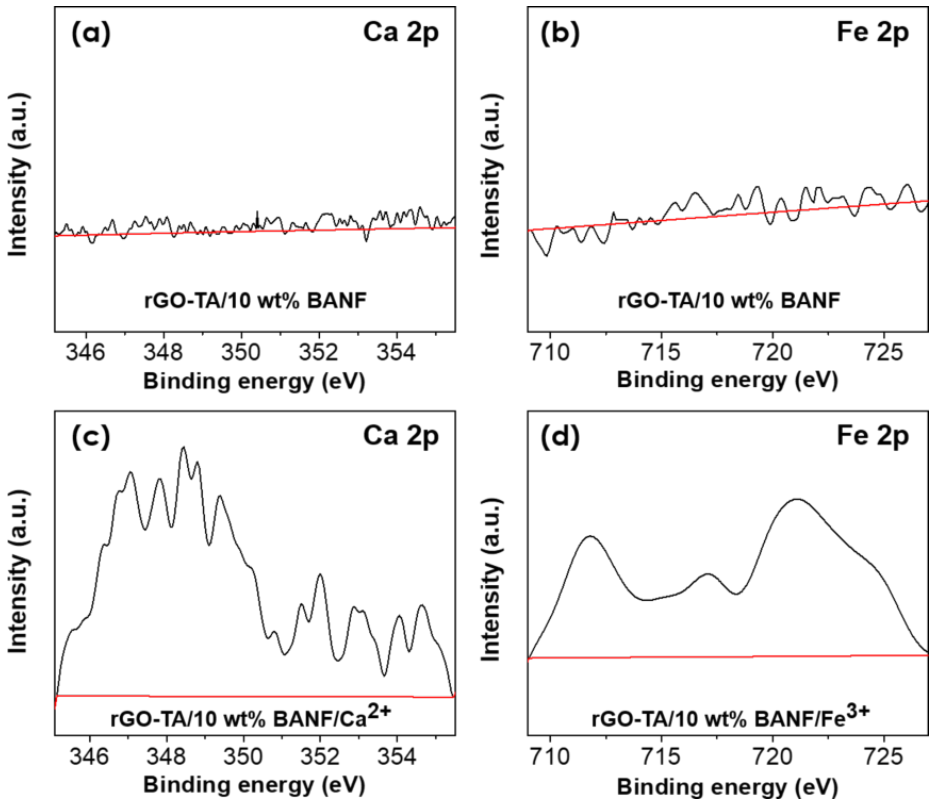

Fig. S3 High resolution XPS (a) Ca 2p and (b) Fe 2p peak for rGO-TA/10 wt% BANF, respectively. High resolution XPS (c) Ca 2p peak rGO-TA/10 wt% BANF/Ca^{2+} and (d) Fe 2p peak for rGO-TA/10 wt% BANF/Fe^{3+}.

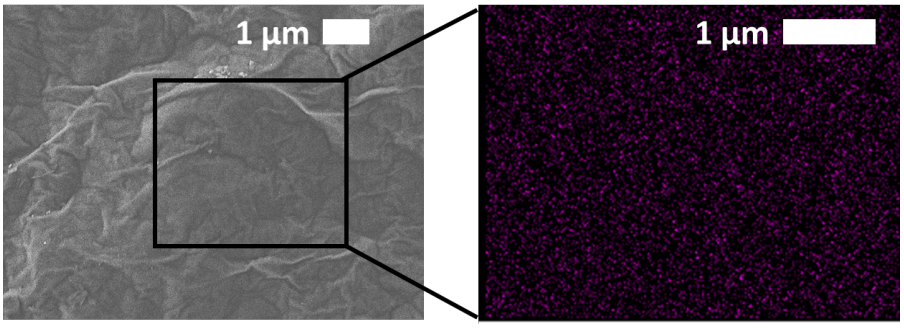

Fig. S4 SEM image and EDS mapping of Fe element for the surface of rGO-TA/10 wt% BANF/Fe^{3+}. Fe is uniformly distributed on the surface of the composite electrodes.

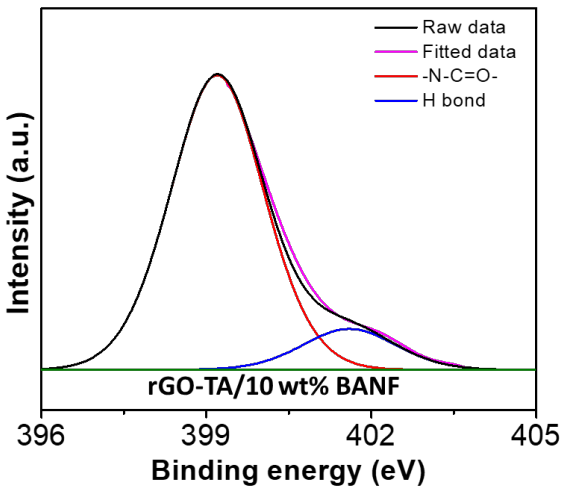

Fig. S5 High resolution XPS N1s peak for rGO-TA/10 wt% BANF. Amide peak at 399.9 eV and H-bond peak at 401.8 eV.

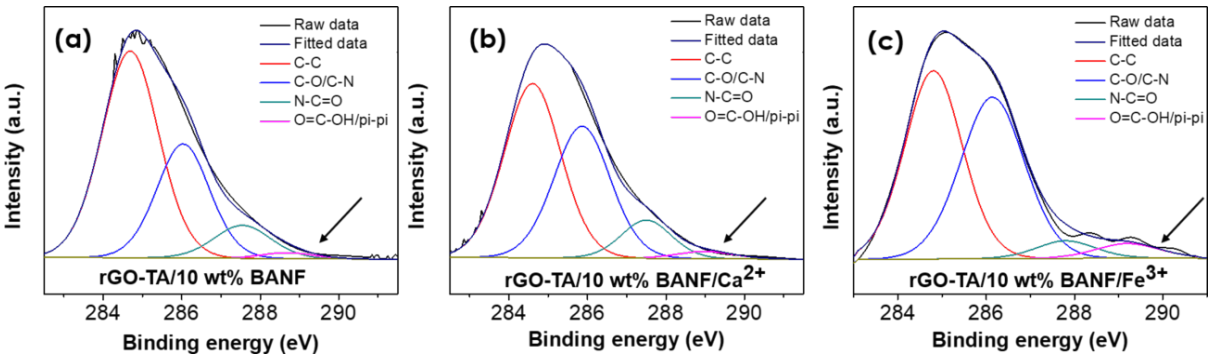

Fig. S6 High resolution C1s XPS peaks for (a) rGO-TA/10 wt% BANF, (b) rGO-TA/10 wt% BANF/Ca^{2+}, and (c) rGO-TA/10 wt% BANF/Fe^{3+}.

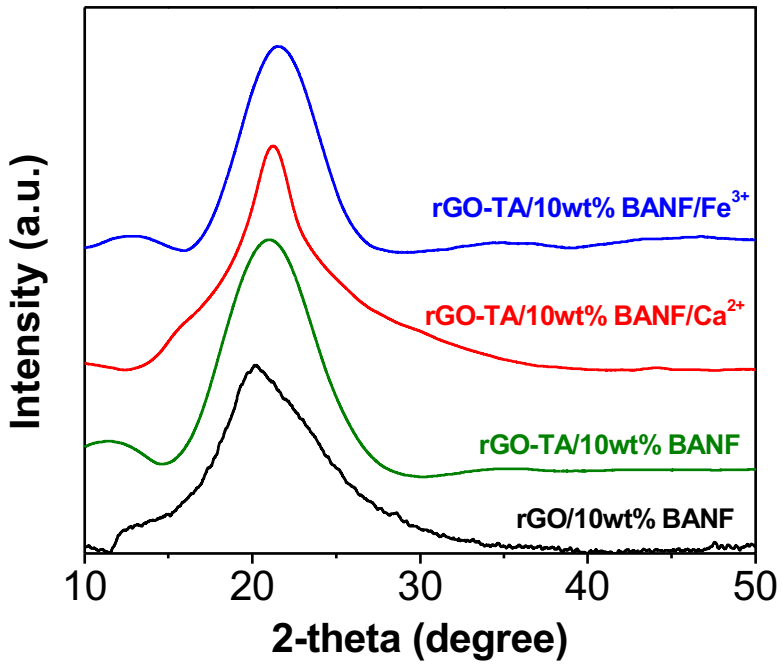

Fig. S7 X-ray diffractograms for rGO-TA/10 wt% BANF, rGO-TA/10 wt% BANF/Ca^{2+}, and rGO-TA/10 wt% BANF/Fe^{3+}. The rGO/10 wt% BANF curve is adapted from ref. 6.

Table S2 X-ray diffraction for rGO, rGO/10 wt% BANF, rGO-TA/10 wt% BANF, rGO-TA/10 wt% BANF/Ca^{2+}, and rGO-TA/10 wt% BANF/Fe^{3+}.

	Theta (º)	**d-spacing (nm)**
rGO [6]	19.9	0.446
rGO/10 wt% BANF [6]	20.2	0.439
rGO-TA/10 wt% BANF	21.0	0.423
rGO-TA/10 wt% BANF/Ca^{2+}	21.3	0.417
rGO-TA/10 wt% BANF/Fe^{3+}	21.5	0.413

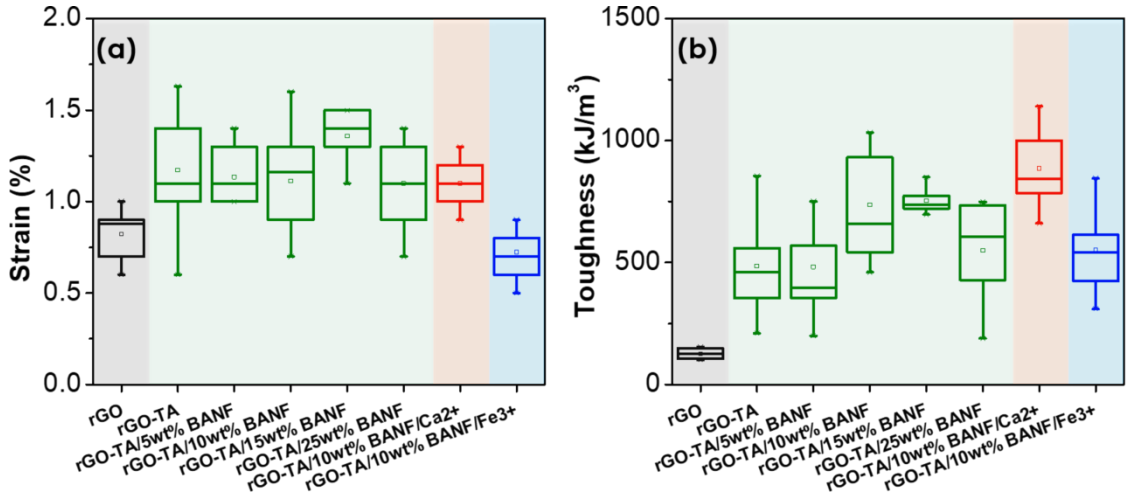

Fig. S8 Box plots of (a) ultimate strain and (b) toughness for the composite films as obtained from tensile testing.

Table S3 Results of tensile testing. Each entry indicates the average and standard deviation of 10-12 samples.

Sample	Young's modulus [GPa]	Ultimate Strength [MPa]	Ultimate strain [%]	Toughness [kJ/m^3]
rGO[5]	5 ± 1	35 ± 6	0.8 ± 0.1	120 ± 30
rGO-TA	9 ± 1	78 ± 6	1.0 ± 0.3	420 ± 130
rGO-TA/5 wt% BANF	12 ± 2	92 ± 18	1.0 ± 0.1	380 ± 220
rGO-TA/10 wt% BANF	17 ± 3	140 ± 20	1.1 ± 0.3	630 ± 230
rGO-TA/15 wt% BANF	15 ± 1	145 ± 7	1.3 ± 0.2	750 ± 50
rGO-TA/25 wt% BANF	11 ± 1	90 ± 15	1.1 ± 0.3	550 ± 200
rGO-TA/10 wt% BANF/Ca^{2+}	19 ± 2	140 ± 8	1.0 ± 0.2	860 ± 200
rGO-TA/10 wt% BANF/Fe^{3+}	25 ± 2	140 ± 18	0.7 ± 0.1	550 ± 150
rGO/10 wt% BANF/Fe^{3+}	12 ± 2	97 ± 8	1.0 ± 0.2	450 ± 80
rGO/Fe^{3+}	6.5 ± 1	40 ± 5	0.6 ± 0.1	130 ± 20

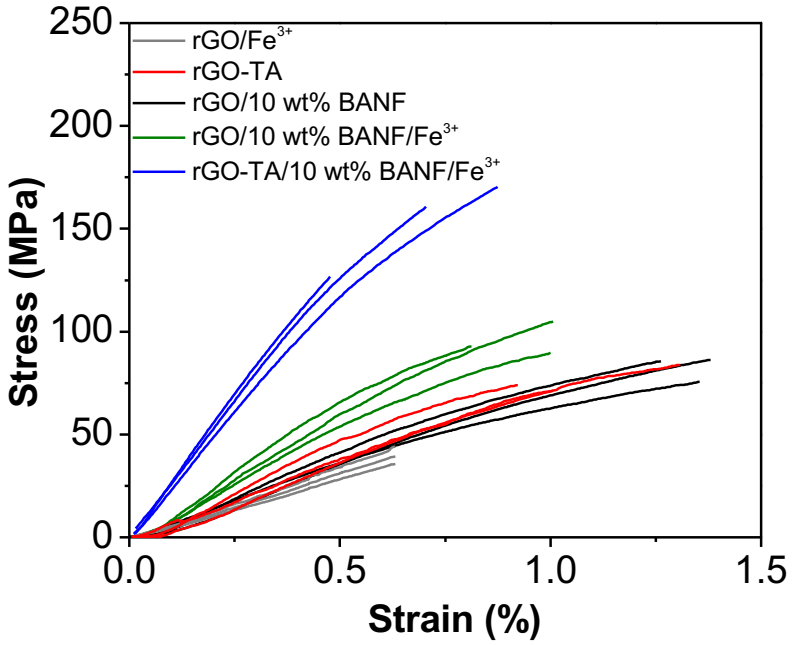

Fig. S9 Typical stress-strain curves for rGO/Fe^{3+}, rGO-TA, rGO/10 wt% BANF, rGO/10 wt% BANF/Fe^{3+}, and rGO-TA/10 wt% BANF/Fe^{3+}. The rGO/10 wt% BANF curves are adapted from ref. 6.

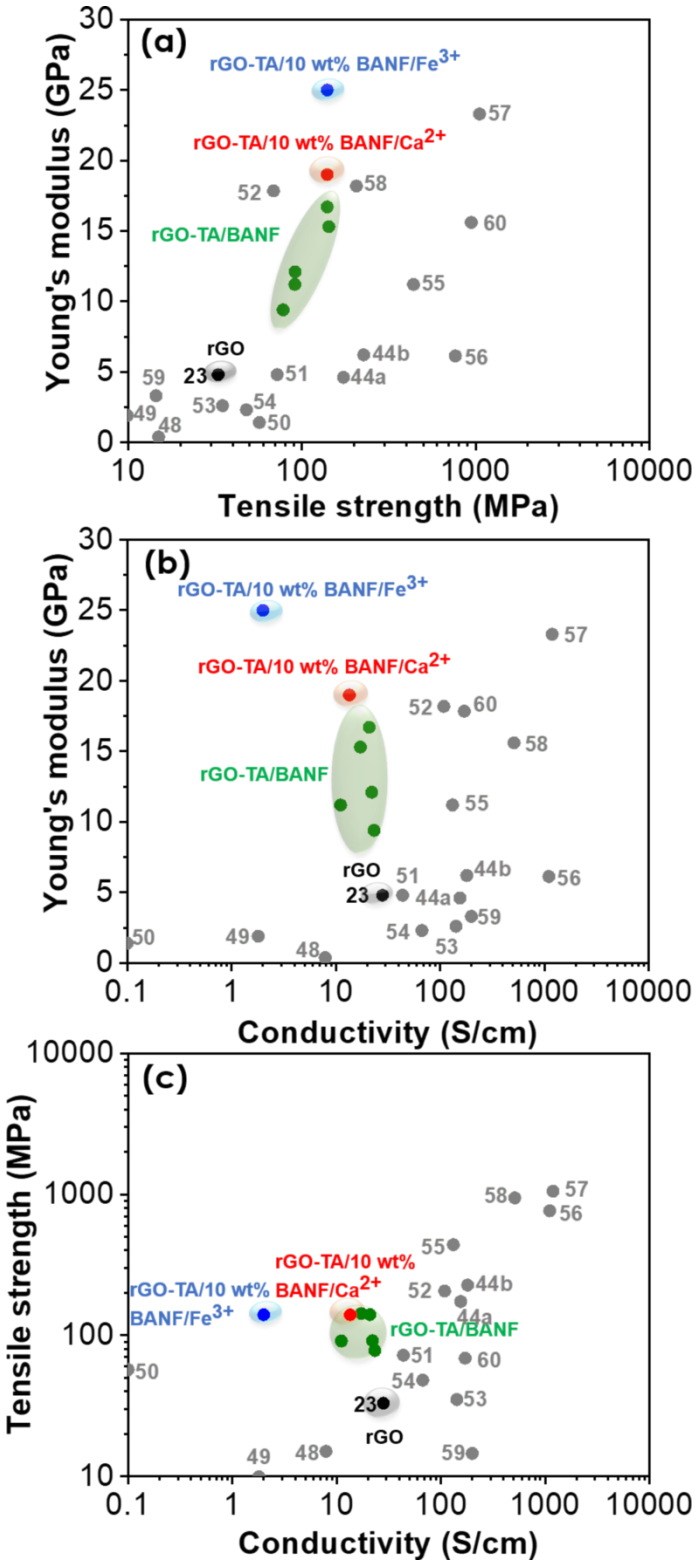

Fig. S10 Ashby plots of (a) Young's modulus *vs.* tensile strength, (b) Young's modulus *vs.* conductivity, and (c) tensile strength *vs.* conductivity for mechanically strong conductive materials. Numbers correspond to references in the main text.

Table S4 Data for Ashby plot (Young's modulus *vs.* tensile strength *vs.* electrical conductivity) for mechanically strong conductive materials.

Ref. no.*	Materials	Young's modulus [GPa]	Electrical conductivity [S/cm]	Tensile strength (MPa)	Fabrication method
48	PPY/cellulose	0.38	7.9	15	Cast on Teflon mould
49	PANI/CNT	1.8	1.9	9.9	Vacuum filtration
50	ANF/PPY	1.4	0.1	57	Vacuum filtration
59	MWCNTs	3.3	200	14.5	Spray layer-by-layer MWNTNH_3^+ /MWNT-COO^- on carbon paper
53	PPY/rGO	2.6	142.1	35	Vacuum filtration
54	rGO/MnO_2/ CNT	2.3	67	48	Vacuum filtration
23	rGO	4.8	28 ± 2	33	Vacuum filtration
51	rGO/Cellulose	4.8	44	72.2	Vacuum filtration
44a	rGO-PDA	4.6	155.3	173.6	Vacuum filtration
44b	rGO-PDA/Ni^{2+}	6.2	180.3	227.1	Vacuum filtration
56	rGO-CNC	6.13	1105	765	Cast-drying
55	rGO-PCO/Zn^{2+}	11.2	131.8	439.1	Vacuum filtration
60	SWCNT-Ppy-CE composite paper	17.84	171	68.73	Ppy deposition on SWCNT buckypaper
52	rGO-PAA	18.2	108.9	206	Vacuum filtration
58	SBG	15.6	512.3	944.5	Vacuum filtration
57	pBG	23.3	1192.2	1054.3	Vacuum filtration
-	**rGO-TA (this study)**	**9 ± 1**	**23 ± 2**	**78**	**Vacuum filtration**
-	**rGO-TA/5 wt% BANF (this study)**	**12 ± 2**	**22 ± 2**	**91.5**	**Vacuum filtration**

-	**rGO-TA/10 wt% BANF (this study)**	**17 ± 3**	**21 ± 1**	**140**	**Vacuum filtration**
-	**rGO-TA/15 wt% BANF (this study)**	**15 ± 1**	**17 ± 1**	**143**	**Vacuum filtration**
-	**rGO-TA/25 wt% BANF (this study)**	**11 ± 1**	**11 ± 1**	**91.1**	**Vacuum filtration**
-	**rGO-TA/10 wt% BANF/Ca^{2+} (this study)**	**19 ± 2**	**14 ± 1**	**140**	**Vacuum filtration**
-	**rGO-TA/10 wt% BANF/Fe^{3+} (this study)**	**25 ± 2**	**2.0 ± 1**	**140**	**Vacuum filtration**

* 'Ref. Number' corresponds to reference number in the main text.

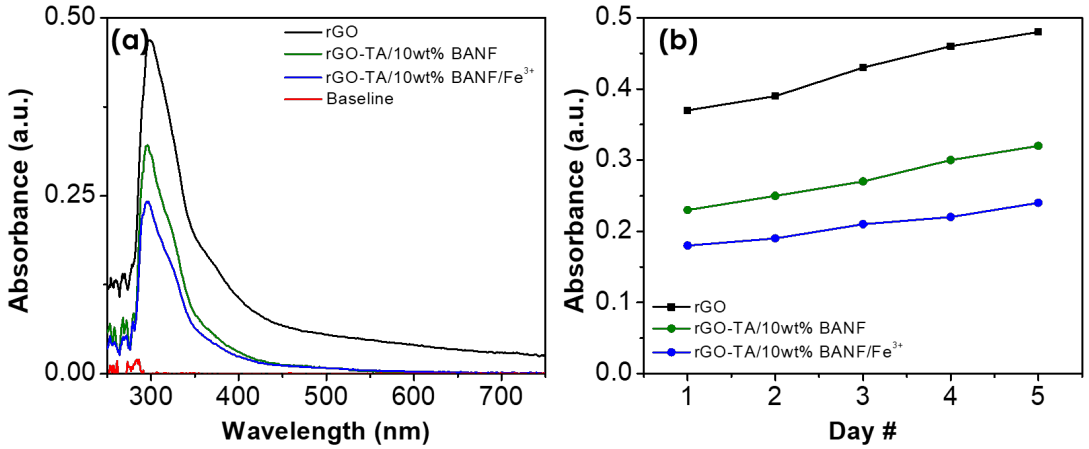

Fig. S11 (a) UV-Vis spectra of day 5 and (b) absorbance at 300 nm *vs.* day number of 6M KOH in contact with rGO, rGO-TA/10 wt% BANF, and rGO-TA/10 wt% BANF/Fe^{3+} electrodes. The rGO/10 wt% BANF curve is adapted from ref. 6. The stability of the electrodes in the electrolyte (6M KOH) was tested using UV-Vis spectroscopy. Each electrode was placed in a vial filled with 2 ml of 6M KOH and the UV-Vis spectra of 1 ml of the electrolyte in contact with each electrode was collected every 24 h. All spectra exhibited a sharp peak at ~300 nm. TA functionalization and Fe^{3+} addition led to lower absorbance values and lower variance in absorbance with time indicating the better stability of these electrodes in the electrolyte.

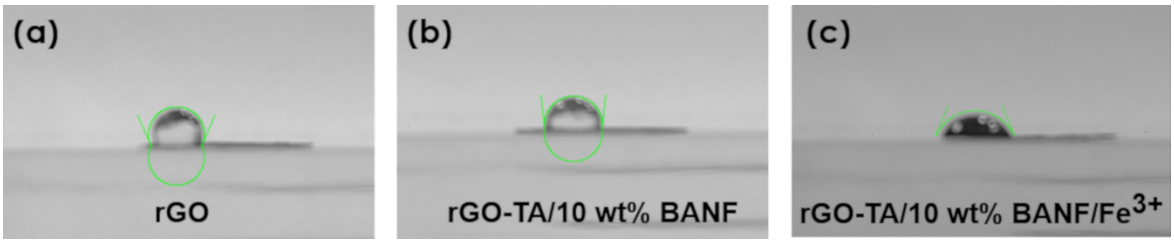

Fig. S12 Contact angle images for (a) rGO, (b) rGO-TA/10 wt% BANF, and (c) GO-TA/10 wt% BANF/ Fe^{3+} electrodes using 10 µl of 6M KOH. Results are summarized in **Table S5**.

Table S5 Contact angle measurements.

Sample	Angle (°)
rGO	102 ± 5
rGO-TA/10 wt% BANF	96 ± 3
rGO-TA/10 wt% BANF/Fe^{3+}	67 ± 5

Table S6 Specific capacitance at varying scan rates from cyclic voltammetry.

Scan rate [V/s]	rGO[5] [F/g]	rGO-TA/10 wt% BANF [F/g]	rGO-TA/10 wt% BANF/Fe^{3+} [F/g]
0.001	216 ± 11	120 ± 8	145 ± 9
0.005	206 ± 6	109 ± 8	120 ± 9
0.01	169 ± 7	98 ± 6	103 ± 8
0.02	169 ± 7	87 ± 7	81 ± 8
0.05	120 ± 10	63 ± 5	45 ± 10
0.07	95 ± 6	52 ± 7	34 ± 7
0.1	83 ± 4	39 ± 8	23 ± 9

Table S7 Cycling stability for 1000 cycles at 0.5 A/g from galvanostatic charge/discharge test.

cycle #	rGO[5] [F/g]	rGO-TA/10 wt% BANF [F/g]	rGO-TA/10 wt% BANF/Fe^{3+} [F/g]
1	212 ± 5	84 ± 6	100 ± 7
10	193 ± 7	77 ± 8	97 ± 7
50	192 ± 6	76 ± 8	96 ± 7
100	190 ± 9	75 ± 9	96 ± 6
200	189 ± 7	75 ± 5	94 ± 7
300	188 ± 7	75 ± 7	94 ± 8
400	187 ± 5	74 ± 9	94 ± 9
500	187 ± 4	74 ± 7	93 ± 8
600	186 ± 5	74 ± 6	92 ± 7
700	185 ± 8	74 ± 6	92 ± 8
800	184 ± 5	74 ± 4	91 ± 9
900	182 ± 7	74 ± 7	91 ± 8
1000	181 ± 8	74 ± 9	91 ± 7

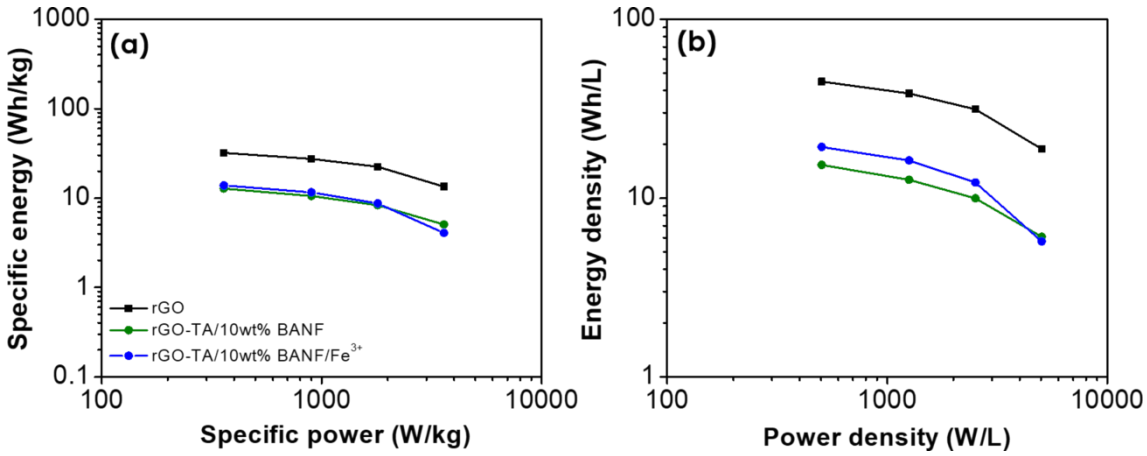

Fig. S13 Ragone plots of (a) Specific energy (Wh/kg) *vs.* specific power (W/kg) and (b) energy density (Wh/L) *vs.* power density (W/L) for rGO, rGO-TA/10 wt% BANF, and rGO-TA/10 wt% BANF/Fe^{3+}.

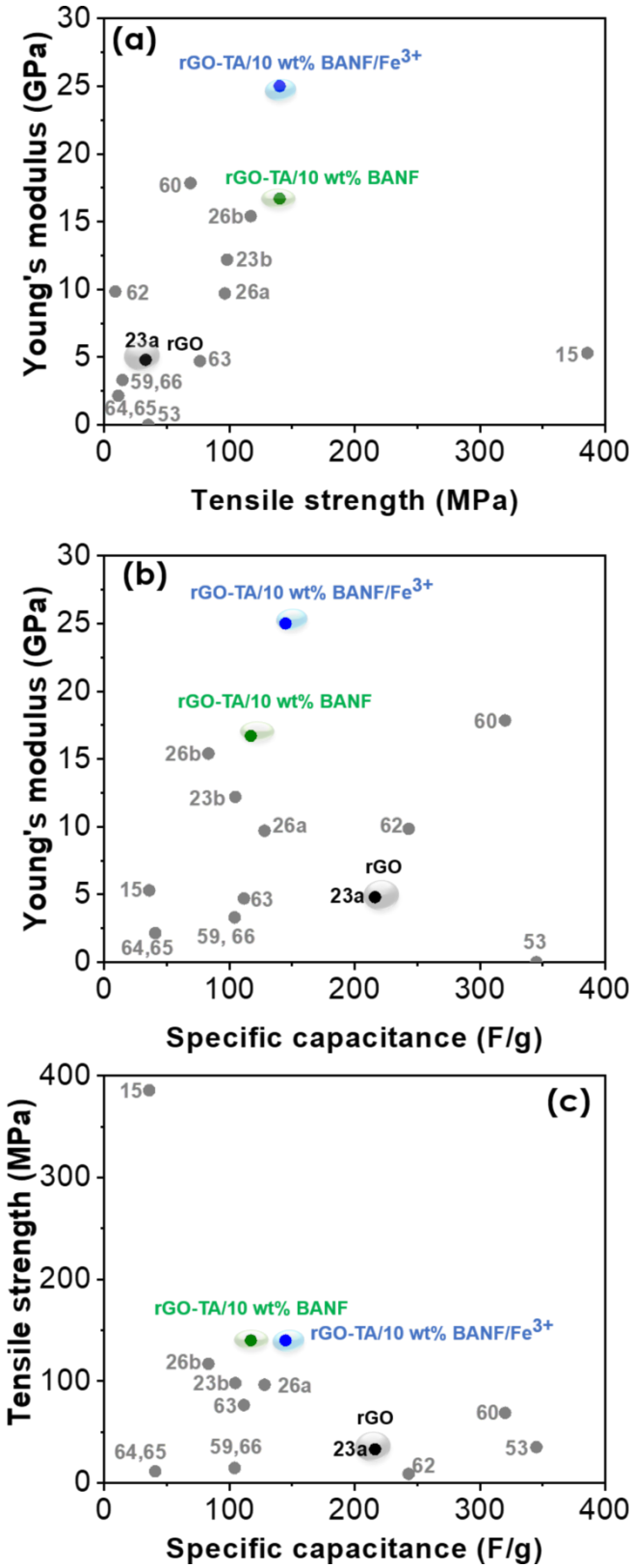

Fig. S14 Ashby plots of (a) Young's modulus *vs.* tensile strength, (b) Young's modulus *vs.* specific capacitance, and (c) tensile strength *vs.* specific capacitance for mechanically strong supercapacitor electrodes. Numbers correspond to references in the main text.

Table S8. Data for Ashby plot (Young's modulus *vs.* tensile strength *vs.* specific capacitance) for mechanically strong supercapacitor electrodes.

					Fabrication method	
Ref. number*	**Materials**	**Young's modulus [GPa]**	**Tensile strength [MPa]**	**Specific Capacitance [F/g]**	**Mechanical**	**Electrochemical**
64, 65	SWCNT paper	2.15	11.2	40.7	Vacuum filtration	
59, 66	MWCNT paper	3.3	14.5	104	Electrophoretically deposited on stainless steel substrate	Spray layer-by-layer $MWNTNH_3^+$ /MWNT-COO^- on carbon paper
23a	rGO	4.8	33	216.2	Vacuum filtration	
63	ANFs/PEDOT:PSS	4.7	76.4	111.5	Vacuum filtration	
62	rGO/MnO_2	9.84	8.79	243	Vacuum filtration, followed by hydrazine reduction	
26a	rGO-1wt% DOPA/10wt% BANF	9.7	96.3	127.9	Vacuum filtration	
23b	rGO-NH_2/25wt% ANF	12	98	105	Vacuum filtration	
15	Wire shaped rGO/CNT composite	5.3	385.7	35.9	Wet spinning of GO/CNT dispersion	
60	SWCNT-Ppy-CE composite paper	17.84	68.7	320	Ppy deposition on SWCNT buckypaper	
26b	rGO-1wt% DOPA/10wt% BANF/Ca^{2+}	15.4	116.9	83.2	Vacuum filtration	
53	PPy/rGO	0.0021	35	345	Vacuum filtration	
-	**rGO-TA/10 wt% BANF (this study)**	**17 ± 3**	**140**	**120 ± 8**	**Vacuum filtration**	
-	**rGO-TA/10 wt% BANF/Fe^{3+} (this study)**	**25 ± 2**	**140**	**145 ± 9**	**Vacuum filtration**	

* 'Ref. Number' corresponds to reference number in the main text.

Table S9 Multifunctional efficiency using carbon aerogel (specific energy: 12.5 Wh/kg) and epoxy (specific Young's modulus: 2.8 GPa·cm^3/g) as the energy storage and structural monofunctional material.[4, 8, 9]

Material	Specific energy (Wh/kg)	Specific Young's modulus (GPa·cm^3/g)	Multifunctional efficiency
rGO[5]	27.0	3.4	3.4
rGO-TA/10 wt% BANF	10.5	24.3	9.5
rGO-TA/10 wt% BANF/Fe^{3+}	11.6	27.8	10.8

* Multifunctional efficiency was calculated as described in ref. 6.

Table S10 Cycling stability for 100 bending cycles at 20 mV/s from cyclic voltammetry test for rGO-TA/10wt% BANF/Fe^{3+}.

cycle #	Specific capacitance [F/g]	
	Flat	**Bent**
1	48.7	44.1
10	47.9	42.4
20	47.9	42.1
30	47.6	41.5
40	47.0	40.9
50	46.8	40.4
60	46.3	39.8
70	46.0	39.2
80	45.9	38.8
90	45.8	38.2
100	45.7	37.8

References

1. W. S. Hummers and R. E. Offeman, *J. Am. Chem. Soc.*, 1958, **80**, 1339-1339.
2. M.-Y. Lim, H. Shin, D. M. Shin, S.-S. Lee and J.-C. Lee, *Polymer*, 2016, **84**, 89-98.
3. J. Zhu, M. Yang, A. Emre, J. H. Bahng, L. Xu, J. Yeom, B. Yeom, Y. Kim, K. Johnson, P. Green and N. A. Kotov, *Angew. Chem. Int. Ed.*, 2017, **56**, 11744-11748.
4. S. R. Kwon, J. Harris, T. Zhou, D. Loufakis, J. G. Boyd and J. L. Lutkenhaus, *ACS Nano*, 2017, **11**, 6682-6690.
5. P. Flouda, X. Y. Feng, J. G. Boyd, E. L. Thomas, D. C. Lagoudas and J. L. Lutkenhaus, *Batteries & Supercaps*, 2019, **2**, 464-472.
6. P. Flouda, S. A. Shah, D. C. Lagoudas, M. J. Green and J. L. Lutkenhaus, *Matter*, 2019, DOI: https://doi.org/10.1016/j.matt.2019.09.017.
7. J. F. Che, P. Chen and M. B. Chan-Park, *J Mater Chem A*, 2013, **1**, 4057-4066.
8. L. L. Zhang and X. S. Zhao, *Chem. Soc. Rev.*, 2009, **38**, 2520-2531.
9. D. Qu and H. Shi, *J. Power Sources*, 1998, **74**, 99-107.